2-Dimensional Transition Metal Dichalcogenides with Tunable Direct Band Gaps: $MoS_{2(1-x)}Se_{2x}$ Monolayers

*John Mann, Quan Ma, Patrick M. Odenthal, Miguel Isarraraz, Duy Le, Edwin Preciado, David Barroso, Koichi Yamaguchi, Gretel von Son Palacio, Andrew Nguyen, Tai Tran, Michelle Wurch, Ariana Nguyen, Velveth Klee, Sarah Bobek, Dezheng Sun, Tony. F. Heinz, Talat S. Rahman, Roland Kawakami, and Ludwig Bartels**

The intense interest in graphene as the prototype 2D electronic material has recently been complemented by the investigation of layered transition metal dichalcogenides (TMD), notably MoS_2 and $MoSe_2$. These materials provide the favorable mechanical properties of graphene, but exhibit a direct bandgap without the need for nanostructuring,[1,2] chemical functionalization,[3] or the application of a strong electric field to bilayers.[4,5] Here we present a simple synthetic route to produce single-layer $MoS_{2(1-x)}Se_{2x}$ films with an arbitrary S/Se ratio. This allows us to tune the direct optical gap continuously between the values of single-layer MoS_2 (1.87 eV) and $MoSe_2$ (1.55 eV).

The electronic structure of 2D TMD monolayers of the form MX_2 (M = Mo, W; X = S, Se) differs significantly from that of graphene. While the latter is a semi-metal with a linear energy dispersion near the K point in the Brillouin zone, the monolayer TMD sheets have direct bandgaps of 1–2 eV, with valence band maxima and conduction band minima at the K point.[6–8] Excitons and charged excitons (trions)[9,10] can be created in TMD monolayers by optical excitation, while the use of circular polarized light has been shown to produce long-lived valley polarization.[11–13] The ability to tune continuously the bandgap of this distinctive class of atomically thin materials through the growth of S/Se alloys opens many new possibilities for basic studies and device concepts. In addition to optimizing the bandgap for applications in electronic and photonic devices made from a single alloy layer, the availability of a class of materials with tunable gaps will also permit the fabrication of novel heterostructures. The impact of such bandgap engineering in traditional III-V semiconductors on both fundamental studies of electron transport and on applications from high-performance transistors to lasers is well known. The recent development of a synthetic route for single-layer $Mo_{1-x}W_xS_2$ material,[14] as well as the investigation of strained MoS_2 (bi-)layers[15,16] were inspired by this objective. Here we show that control of the chalcogen composition allows a wider tuning range of the bandgap. Using the capabilities for alloy growth presented in this paper, the formation of both vertical and lateral heterostructures of monolayers of $MoS_{2(1-x)}Se_{2x}$ of differing composition should be possible.

Several methods have been developed to prepare atomically thin films of MoS_2 that complement the exfoliation of bulk crystals. These approaches include chemical vapor deposition (CVD) using $MoCl_5$ or MoO_3 and S as sources,[17–20] laser-based thinning,[21] plasma thinning,[22] liquid exfoliation,[23–26] graphene assisted growth,[27] and the sulfurization of molybdenum films prepared by e-beam deposition[28] or dip coating.[29] Thicker films of MoS_2 and $MoSe_2$[30] have been grown by numerous CVD techniques. For growth of monolayers of MoS_2, the methods typically lead to single-layer triangular or hexagonal islands several microns in size, as well as to elongated areas of single-layer film on the order of 100 microns in length.

In our synthesis, we make use of organic precursors for both sulfur and selenium, combined with the MoO_3 as a source for molybdenum. We use thiophenol dissolved in tetrahydrofuran as sulfur source and add diphenyl-diselenide to the solution to adjust the sulfur/selenium ratio. We place the growth substrate, typically a Si(110) wafer covered by a 300 nm SiO_2 layer, in the center of a tube furnace. The substrate can be positioned directly on top of a boat carrying MoO_3 powder. Alternatively, in order to achieve more homogeneous films, we can support the substrate by a Mo-mesh above a flat Mo shim covered by MoO_3 powder (typically: 0.3 g). (**Figure 1**a provides a schematic representation of the growth system, a photograph of which is included in the supporting material.) Growth is achieved by injecting the liquid chalcogen source (~ 1mL) via a long syringe needle near the process region of the tube furnace at 650–700 °C and then immediately switching off the heating of the furnace. Growth has been achieved over a temperature range of 50 °C using tube furnaces with both 1″ and 2″ process tubes. Both the oxygenate solvents and post-growth (after the furnace has cooled to 500 °C) application of H_2 gas are necessary to avoid

J. Mann, Q. Ma, P. M. Odenthal, M. Isarraraz,
E. Preciado, D. Barroso, K. Yamaguchi,
G. von Son Palacio, A. Nguyen, T. Tran,
M. Wurch, A. Nguyen, V. Klee, S. Bobek,
D. Sun, R. Kawakami, L. Bartels
Chemistry, Physics, Electrical Engineering and
Materials Science and Engineering
University of California
Riverside, CA, 92521, USA
E-mail: Ludwig.Bartels@ucr.edu

D. Le, T. S. Rahman
Department of Physics
University of Central Florida
Orlando, FL, 32816, USA

D. Sun, T. F. Heinz
Departments of Physics and Electrical Engineering
Columbia University
New York, NY, 10027, USA

DOI: 10.1002/adma.201304389

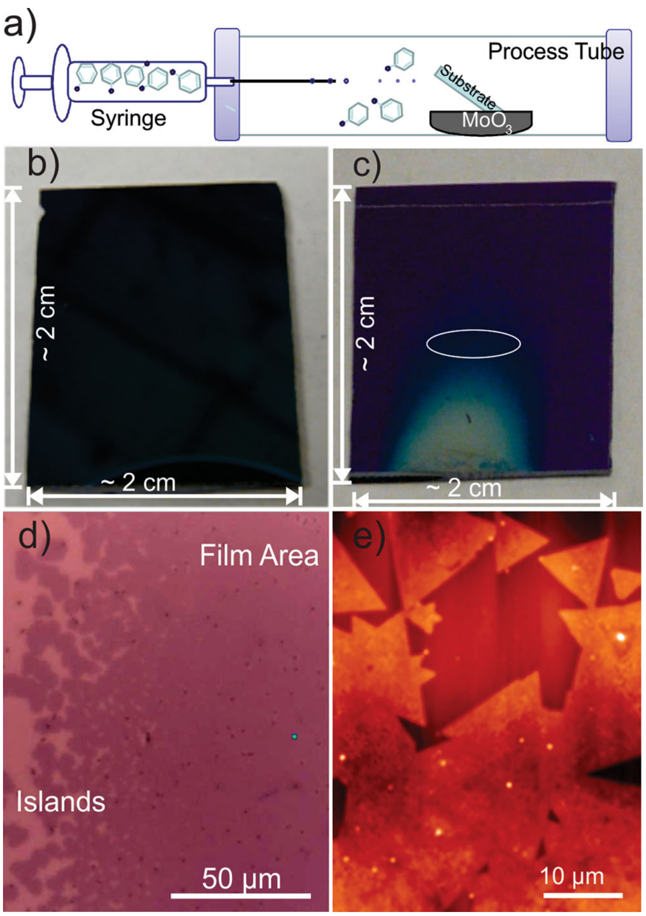

Figure 1. a) Schematic representation of the growth process. A substrate is suspended above MoO_3 powder in a tube furnace heated to 650–700 °C in nitrogen, at which point the liquid chalcogen precursors are injected. b,c) Optical images of MoS_2 and $MoSe_2$ films, respectively. A single-layer MoS_2 film covers the entire substrate, except the dark area at the bottom. Homogeneous single-layer growth of $MoSe_2$ is found in the circled area of the substrate, with the purple area being empty and the bright area carrying a thick film. d) optical micrograph of the area near an edge of a $MoS_{2(1-x)}Se_{2x}$ film with 1.8 eV optical bandgap. On the left, individual (mostly triangular) islands are visible. On the right, the film becomes continuous and presumably contains many rotational domains. e) representative AFM image of the area near the edge of an alloy film showing triangular single-layer islands (top, ~0.8 nm in height) that merge into a continuous film (bottom).

formation of a carbonaceous deposit on the metal dichalcogenide monolayer. The presence of such a carbonaceous layer is revealed by Raman spectroscopy and causes quenching of the film's photoluminescence (PL) (although Raman spectroscopy indicates that a monolayer TMD film is formed). Photographs of the 2 cm × 2 cm SiO_2/Si substrates (that we typically use in film growth) with MoS_2 and $MoSe_2$ films are shown in Figure 1b,c.

The sulfur-rich TMDs films are found to grow as single layers of larger lateral extent than selenium-rich ones, with pure $MoSe_2$ yielding the smallest single-layer films. The growth process favors sulfur incorporation; thus, the Se:S ratio in the source solution needs to exceed that of the desired film composition. For instance, our $MoS_{1.69}Se_{0.31}$ sample (vide infra) was grown using a Se:S mole fraction of 1:0.7.

Figure 1d,e shows optical and atomic force microscopy (AFM) images of the resultant films, which resemble those found in prior CVD growth of MoS_2.[17–20,31] Because of the growth on an insulating substrates and our lack of a selenium-compatible transfer method, no electron microscopy is available.

Figure 2a shows room-temperature (RT) PL spectra for a series of $MoS_{2(1-x)}Se_{2x}$ films of different composition. These measurements were performed using a laser operating at a wavelength of 532 nm (Coherent Verdi), a spectrometer with a 1200 lines/mm grating, and a liquid-nitrogen cooled CCD detector (Princeton Instruments SPEC-10). The samples range from pure MoS_2, with a PL emission peak at 1.87 eV, to pure $MoSe_2$, with a PL peak at 1.54 eV. The spectra reveal reasonably sharp and bright PL features. We only evaluated sample areas that show strong PL indicative of monolayer films. The chemical composition of the samples is obtained from the relative intensity of the S 2p and Se 3p features measured using X-ray photoelectron spectroscopy (XPS). The XPS measurements are performed with excitation by Al-K_α radiation. The emitted electrons are analyzed by a hemispheric analyzer (Scienta R300), which has a spatial acceptance of 0.7 mm × 0.5 mm. Because of uncertainty in the alignment of the XPS spot with the center of the homogeneous area of the film, we estimate an uncertainty of $\Delta x = \pm 0.1$ in the inferred composition of the $MoS_{2(1-x)}Se_{2x}$ alloys

The variation of the optical gap with the composition of the $MoS_{2(x-1)}Se_{2x}$ alloy monolayers is presented in Figure 2b. The results are based on the A exciton emission energy in PL spectra such as those in Figure 2a. We find a monotonic increase of the optical gap with the fraction of sulfur in the film.

In order to understand the possible microstructure of our films, we perform density functional theory (DFT) calculations using supercells consisting of (6 × 6) TMD unit cells in a periodic arrangement (further details in the supporting information). For each sulfur-to-selenium ratio, we set up supercells that place the sulfur and selenium atoms in different relative locations on both the top and bottom chalcogen plane; we then identify the arrangement with the lowest formation energy. Most of $MoS_{2(1-x)}Se_{2x}$ structures are found to have a very slight negative formation energies (for $x = 1/3$, $1/2$, and $2/3$, the formation energies are the lowest at −6, −7, and −5 meV per $MoS_{2(1-x)}Se_{2x}$ unit), indicating the preference for these structures over the segregation of MoS_2 and $MoSe_2$ even at zero temperature. This behavior has been analyzed in detail in earlier studies.[32,33] Given the influence of entropy, random alloys are expected to be highly stable at elevated temperatures. Phonon frequencies at the Brillioun zone center for the cases $x = 1/3$, $1/2$, and $2/3$ calculated with VASP[34] and Phonopy[35] codes confirm the absence of unstable modes, again indicating that the $MoS_{2(1-x)}Se_{2x}$ alloy structures are stable against phase separation.

For each optimized structure, we calculate the electronic band structure to find a direct band gap for all cases. As in prior DFT work,[32] our calculations underestimate the band gap (MoS_2: 1.68 eV/1.55 eV, $MoSe_2$: 1.45 eV/1.28 eV excluding/including spin-orbit interactions). The calculations, we note,

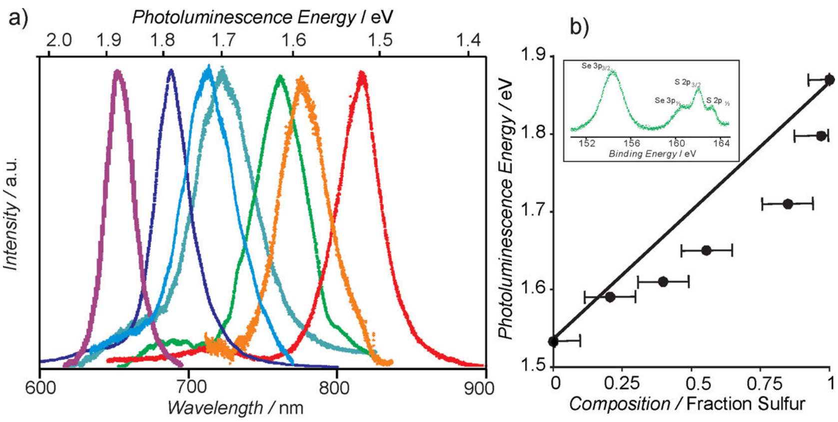

Figure 2. (a) Normalized RT PL spectra for $MoS_{2(1-x)}Se_{2x}$ films of different composition. (b) Variation of the photon energy of the PL emission peak as a function of sample composition, as determined by XPS. (The inset shows a representative XPS spectrum of the Se 3p and S 2p peaks). The black line indicates a linear variation between the values of the stoichiometric compounds as found in our DFT calculations.

also omit excitonic corrections, which are relevant for the experimental optical transition energies. The computed band gaps scale approximately linearly with the S/Se ratio, both with and without the inclusion of spin-orbit interactions (see supporting material). Although the numerical values of the gaps do not agree quantitatively with the stoichiometric compounds, we expect the linear variation with alloy composition to be a robust result. We have accordingly represented the theoretical prediction by a linear variation (Figure 2b) between the experimental values of the optical bandgaps of MoS_2 and $MoSe_2$. We note that the statistical distribution of chalcogen atoms in the material may contribute to the observed deviation from a linear behavior in the PL emission energies with composition. In lower-dimensional materials like our 2D films, such statistical fluctuations are typically more significant than in 3D alloys. In particular, the finite diffusion length of the excitons[18] may lead to emission being enhanced from regions of the film with high local Se content (due to statistical variations) and a reduced effective bandgap. (See supporting material.)

To further examine the homogeneity of the grown films, we obtained spatial maps of the optical emission spectra of several samples of different composition. The measurements were performed using a Horiba LabRam instrument with 10x/100x objectives for mapping of areas larger/smaller than 50 µm × 50 µm, respectively. **Figure 3**a shows a typical set of PL spectra acquired on a 5 µm grid across a 20 µm × 20 µm area. No meaningful variation is observed. To extract the optical bandgap from the spectra, we subtract a linear background and fit the emission peak to a Gaussian form. The resulting spatial maps are displayed in a false color representation in Figure 3b for alloy films of three different compositions. On the scale of the overall tuning range of the optical bandgap, virtually no spatial variation is discernible. The emission map of Figure 3c provides higher energy resolution and shows the variation of the optical bandgap across regions of 70 µm × 70 µm area (top) and a 5 µm × 5 µm (bottom) size. We find a mean value of 1.713 eV and a variation of ±2 meV for the data on the larger spatial scale, for which the excitation spot size was ~5 µm in diameter. For the map with finer (0.5 µm) spatial resolution, we observe a variation of ±5 meV in the emission energy. Several factors may contribute to the variation in emission energy, including substrate-induced changes in doping or strain. If we attribute the entire variation to changes in local alloy composition, then based on the near-linear variation of the bandgap with composition (Figure 2b), the PL results would imply a ±1% compositional variation on the larger and ±3% variation on the finer length scale.

The PL maps shown in Figure 3c at higher spatial resolution (lower panel) appear to reveal the presence of individual crystalline domains of the monolayer film. These grains exhibit dimensions on the micron scale, in agreement with the AFM images in Figure 1e. To characterize this aspect of the alloy film further and to refine our results on the local variation of the PL emission energy, we also investigated the peripheral region of the alloy film where individual monolayer islands are readily identified in optical contrast images (**Figure 4**a). In this region,

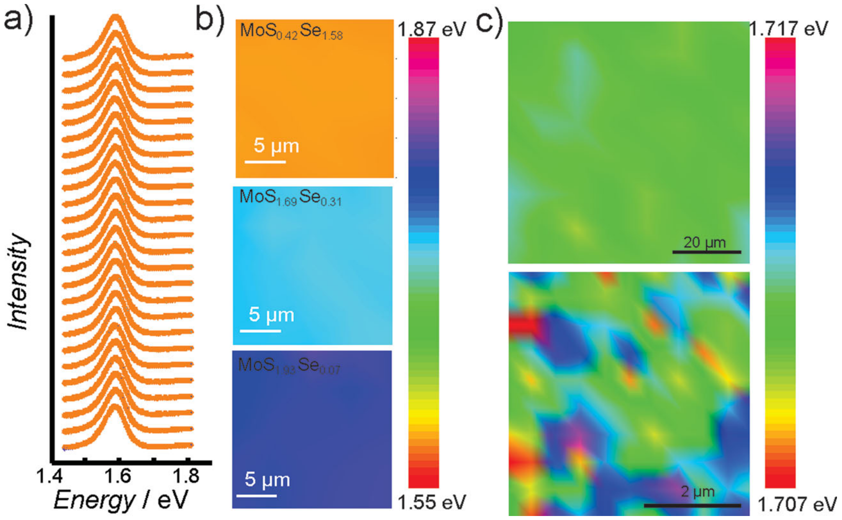

Figure 3. (a) PL spectra obtained on a regular grid across a 20 µm × 20 µm area of a $MoS_{0.42}Se_{1.58}$ alloy monolayer. (b) False color spatial maps of the optical bandgap obtained by fitting PL spectra like those in (a) with a Gaussian function. Compared to the range of achievable optical band gaps, no meaningful spatial variation in the emission energy is observed. (c) The spatial variation of the optical bandgap across a 70 µm × 70 µm area (top) and a 5 µm × 5 µm area (bottom) on a $MoS_{1.69}Se_{0.31}$ film using a spot sizes of ~5 µm and 0.5 µm, respectively. On the larger scale the variation is ±2 meV; this would corresponds to ~ ±1% of variation in composition. On the finer scale, where individual crystalline domains are visible, the variation is ± 5 meV (~ ±3 % variation in composition).

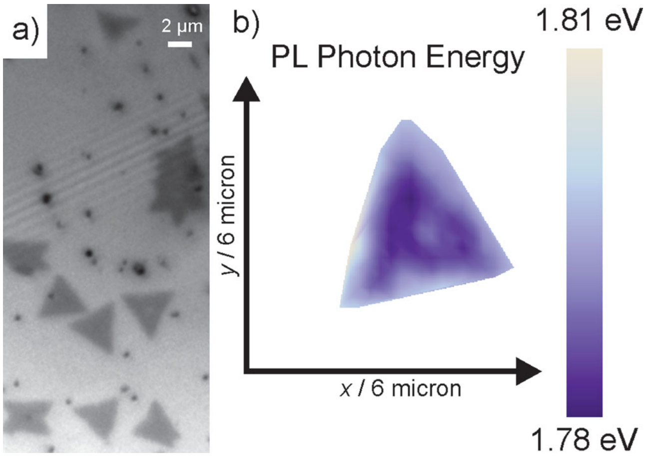

Figure 4. a) Optical image of several triangular islands adjacent to the $MoS_{2(1-x)}Se_{2x}$ film in Figure 1. b) Spatial mapping of the PL emission energy of one of the islands, as measured with 200 nm step size using a 100x objective and 532 nm excitation. The island exhibits the lowest photon energy at its center, which rises slightly toward the perimeter. The color scale corresponds to a variation of 30 meV in the emission photon energy.

the growth consists primarily of individual triangular islands of several microns in size. In accordance with previous studies on CVD films of MoS_2,[18] we associated these islands with single-crystal domains. Figure 4b provides a spatial map of the PL center energy obtained for a single triangular island. We find that the overall PL energy of the island closely matches that of the adjacent film. There is a slightly increased/decrease of PL photon energy at the outside edges and inside of the island (±15 meV), respectively. The presence of isolated edges, absent in the continuous films, may enhance the variation in the PL emission energy for the islands. In any case, fluctuations of ±2 meV, ±5 meV, or even ±15 meV represent a small fraction of the total tuning range of 320 meV and are indicative of the large-scale homogeneity and the absence of significant phase segregation in our films.

As a further characterization of our alloy films, we have measured the temperature dependence of the PL. The $MoS_{0.42}Se_{1.58}$ monolayer of **Figure 5** exhibits typical behavior, with the optical gap E_g decreasing with temperature. The results can described using the semi-empirical formula of O'Donnell et al.[36](1):

$$E_g(\mathrm{T}) = E_g(\mathrm{T}=0) - S\langle\hbar\omega\rangle[\coth(\langle\hbar\omega\rangle/2k_BT) - 1 \qquad (1)$$

The fit to Equation 1 implies an optical band gap at zero temperature $E_g(T = 0) = 1.70$ eV, an electron-phonon-coupling parameter of $S = 1.98$, and an average acoustic phonon energy of $<\hbar\omega> = 17.0$ meV for $MoS_{0.42}Se_{1.58}$. These values compare reasonably with the results for pure MoS_2 (1.86 eV, 1.82 and 22.5 meV) and $MoSe_2$ (1.64 eV, 1.93, 11.6 meV) reported by Tongay *et al.*[37].

We have measured Raman spectra of films of different compositions (**Figure 6**a) by means of the same instrument and excitation wavelength (532 nm) as used for the PL measurements. The experimental Raman spectra of the $MoS_{2(1-x)}Se_{2x}$ monolayer films show two distinct sets of features, with one set related to MoS_2-like E_{2g} and A_{1g} modes at around 400 cm^{-1} and the other set related to the corresponding $MoSe_2$-like features near 240 cm^{-1}.

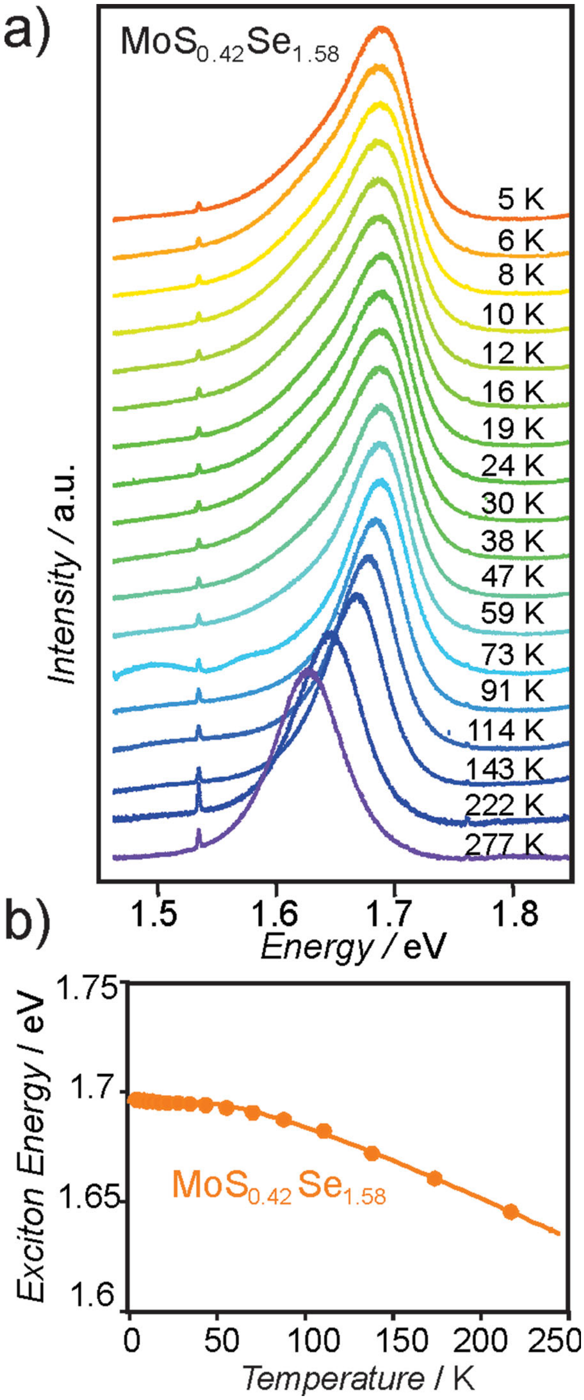

Figure 5. (a) PL spectra for a $MoS_{0.42}Se_{1.58}$ film (orange in Figure 2a) at different temperatures between 277 and 5 K. All spectra are scaled to the same height. (b) The exciton emission energy as a function of the temperature of the film. The fit (solid line) is described in the text.

Unlike the bandgap, which is expected to vary smoothly with composition, the vibrational behavior of alloys is seen to be more complex than that of the stoichiometric compounds. The spectra represent typical "two-mode behavior" (2MB)[38] and do not imply phase separation. Similar behavior is observed in the S/Se alloy of CdS_xSe_{1-x},[39,40] as well as in well-studied alloys such

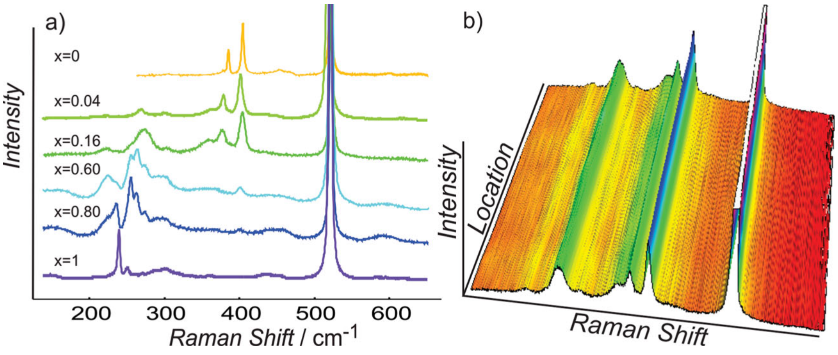

Figure 6. a) Raman spectra measured for $MoS_{2(1-x)}Se_{2x}$ films of different selenium content x. The pronounced feature near 520 cm^{-1} arises from the SiO_2 substrate vibrations. While the peak patterns for the pure materials are simple and sharp, the patterns for alloy films are broader and more complex. The evolution is understood in terms of two-mode behavior, as discussed in the text. b) Three-dimensional representation of the Raman spectra as a function of location on a 0.5 µm grid covering the same location as the bottom part of Figure 3c.

as AlInAs,[41] InGaP,[42] Si-Ge[43] and $Al_xIn_{(1-x)}N$.[44] 2MB occurs when the frequencies of phonon modes in the pure AB and AC compounds differ sufficiently in frequency from one another. For the present case of $MoS_{2(1-x)}Se_{2x}$,, the strong phonon features are shifted from one another by ~200 cm^{-1} in the two pure compounds, which is sufficient for 2MB. For the case of $Mo_{(1-x)}W_xS_2$ alloys, for which the corresponding difference is less than 50 cm^{-1}, one observes "one-mode behavior" with a continuous shift of phonon frequencies with composition.[45]

We have also performed spatial mapping of the Raman response across the area shown in the bottom of Figure 3c (i.e., over a grid at 0.5 µm spacing). Figure 6b is the hypersurface created by plotting the Raman spectra against a coordinate indicating the spatial location on the sample. The spectra are normalized to the intensity at 400 cm^{-1}; the pronounced feature on the right is the substrate SiO_2 mode. No meaningful variation of the Raman spectra with position is discernible, in good agreement with the homogeneity found for the PL signal in Figure 3c.

In conclusion, we have shown the ability to grow alloy monolayer films of $MoS_{2(1-x)}Se_{2x}$ of arbitrary composition through control of the S/Se ratio of the organic precursors used in the growth process. Photoluminescence, Raman, and AFM measurements show a high degree of homogeneity of the films, and theoretical studies strongly support the stability of the alloy films against phase separation. The band structure of the alloy films can be tuned continuously with composition, and both the experimental and theoretical studies show that the material exhibits a direct gap for all alloy compositions. The room-temperature optical bandgap is found to vary smoothly between the limits of 1.87 eV (for pure single-layer MoS_2) and 1.55 eV (for pure single-layer $MoSe_2$). Future studies will address the electrical transport properties of monolayer $MoS_{2(1-x)}Se_{2x}$ films of different composition.

Supporting Information

Supporting Information is available from the Wiley Online Library or from the author.

Acknowledgements

L. B. and R. K. gratefully acknowledge support by C-SPIN, one of six centers supported by the STARnet phase of the Focus Center Research Program (FCRP), a Semiconductor Research Corporation program sponsored by MARCO and DARPA. Work of the Bartels and Heinz groups on the film growth was supported by the US National Science Foundation under grants DMR-1106210 and DMR-1106172, respectively. XPS analysis and theoretical modeling of the films were made possible by a grant by the US Department of Energy (UCR, UCF, Columbia University: DE-FG02–07ER15842). DFT simulations are performed using computational resources provided by the Extreme Science and Engineering Discovery Environment (project TG-DMR130009).

Received: September 1, 2013
Revised: October 14, 2013

[1] M.-W. Lin, C. Ling, Y. Zhang, H. J. Yoon, M. M.-C. Cheng, L. A. Agapito, N. Kioussis, N. Widjaja, Z. Zhou, *Nanotechnology* **2011**, *22*, 265201.
[2] M. Y. Han, B. Özyilmaz, Y. Zhang, P. Kim, *Phys. Rev. Lett.* **2007**, *98*, 206805.
[3] R. Balog, B. Jorgensen, L. Nilsson, M. Andersen, E. Rienks, M. Bianchi, M. Fanetti, E. Laegsgaard, A. Baraldi, S. Lizzit, Z. Sljivancanin, F. Besenbacher, B. Hammer, T. G. Pedersen, P. Hofmann, L. Hornekaer, *Nat. Mater.* **2010**, *9*, 315–319.
[4] Y. Zhang, T.-T. Tang, C. Girit, Z. Hao, M. C. Martin, A. Zettl, M. F. Crommie, Y. R. Shen, F. Wang, *Nature* **2009**, *459*, 820–823.
[5] K. F. Mak, C. H. Lui, J. Shan, T. F. Heinz, *Phys. Rev. Lett.* **2009**, *102*, 256405.
[6] A. Kuc, N. Zibouche, T. Heine, *Phys. Rev. B* **2011**, *83*, 245213.
[7] K. F. Mak, C. Lee, J. Hone, J. Shan, T. F. Heinz, *Phys. Rev. Lett.* **2010**, *105*, 136805.
[8] A. Splendiani, L. Sun, Y. B. Zhang, T. S. Li, J. Kim, C. Y. Chim, G. Galli, F. Wang, *Nano. Lett.* **2010**, *10*, 1271–1275.
[9] K. F. Mak, K. He, C. Lee, G. H. Lee, J. Hone, T. F. Heinz, J. Shan, *Nat. Mater.* **2012**, *12*, 207–211.
[10] J. S. Ross, S. F. Wu, H. Y. Yu, N. J. Ghimire, A. M. Jones, G. Aivazian, J. Q. Yan, D. G. Mandrus, D. Xiao, W. Yao, X. D. Xu, *Nat.Commun.* **2013**, *4* doi:10.1038/ncomms2498.
[11] K. F. Mak, K. He, J. Shan, T. F. Heinz, *Nat. Nano* **2012**, *7*, 494–498.
[12] H. Zeng, J. Dai, W. Yao, D. Xiao, X. Cui, *Nat. Nano* **2012**, *7*, 490–493.
[13] S. Wu, C. Huang, G. Aivazian, J. S. Ross, D. H. Cobden, X. Xu, *Acs Nano* **2013**, *7*, 2768–2772.
[14] D. O. Dumcenco, H. Kobayashi, Z. Liu, Y.-S. Huang, K. Suenaga, *Nat. Commun.* **2013**, *4*, 1351.
[15] H. J. Conley, B. Wang, J. I. Ziegler, R. F. Haglund, S. T. Pantelides, K. I. Bolotin, *Nano Lett..* **2013**, *13*, doi.org/10.1021/nl4014748.
[16] K. He, C. Poole, K. F. Mak, J. Shan, *Nano Lett..* **2013**, *13*, 2931–2936.
[17] Y.-H. Lee, X.-Q. Zhang, W. Zhang, M.-T. Chang, C.-T. Lin, K.-D. Chang, Y.-C. Yu, J. T.-W. Wang, C.-S. Chang, L.-J. Li, T.-W. Lin, *Adv. Mater.* **2012**, *24*, 2320–2325.
[18] A. M. v. d. Zande, P. Y. Huang, D. A. Chenet, T. C. Berkelbach, Y. You, G. H. Lee, T. F. Heinz, D. R. Reichman, D. A. Muller, *J. Hone Nat. Mater.* **2013**, *12*, 554–561.
[19] Yifei Yu, Chun Li, Yi Liu, Liqin Su, Y Zhang, L. Cao, *Sci. Reports* **2013**, *3*, 1866.

[20] S. Najmaei, Z. Liu, W. Zhou, X. Zou, G. Shi, S. Lei, B. I. Yakobson, J.-C. Idrobo, P. M. Ajayan, J. Lou, *Nat. Mater. 12*, 754.

[21] A. Castellanos-Gomez, M. Barkelid, A. M. Goossens, V. E. Calado, H. S. J. van der Zant, G. A. Steele, *Nano Lett.*. **2012**, *12*, 3187.

[22] Y. Liu, H. Nan, X. Wu, W. Pan, W. Wang, J. Bai, W. Zhao, L. Sun, X. Wang, Z. Ni, *Acs Nano* **2013**, *7*, 4202.

[23] G. Eda, H. Yamaguchi, D. Voiry, T. Fujita, M. Chen, M. Chhowalla, *Nano Lett.* **2011**, *11*, 5111–5116.

[24] A. O'Neill, U. Khan, J. N. Coleman, *Chem Mater* **2012**, *24*, 2414–2421.

[25] Z. Zeng, Z. Yin, X. Huang, H. Li, Q. He, G. Lu, F. Boey, H. Zhang, *Angew. Chem. Int. Ed. Engl.* **2011**, *50*, 11093–11097.

[26] K. Lee, H.-Y. Kim, M. Lotya, J. N. Coleman, G.-T. Kim, G. S. Duesberg, *Adv. Mater.* **2011**, *23*, 4178–4182.

[27] Y. Shi, W. Zhou, A.-Y. Lu, W. Fang, Y.-H. Lee, A. L. Hsu, S. M. Kim, K. K. Kim, H. Y. Yang, L.-J. Li, J.-C. Idrobo, J. Kong, *Nano Lett.* **2012**, *12*, 2784–2791.

[28] Y. Zhan, Z. Liu, S. Najmaei, P. M. Ajayan, J. Lou, *Small* **2012**, *8*, 966–971.

[29] K.-K. Liu, W. Zhang, Y.-H. Lee, Y.-C. Lin, M.-T. Chang, C.-Y. Su, C.-S. Chang, H. Li, Y. Shi, H. Zhang, C.-S. Lai, L.-J. Li, *Nano Lett.* **2012**, *12*, 1538–1544.

[30] N. D. Boscher, C. J. Carmalt, R. G. Palgrave, J. J. Gil-Tomas, I. P. Parkin, *Chem.Vap. Dep.* **2006**, *12*, 692–698.

[31] J. Mann, D. Sun, Q. Ma, E. Preciado, K. Yamaguchi, J.-R. Chen, T. F. Heinz, R. Kawakami, L. Bartels, *Europ. Phys. J. B* **2013**, *86*, 226.

[32] J. Kang, S. Tongay, J. Zhou, J. B. Li, J. Q. Wu, *Appl. Phys. Lett.* **2013**, *102*, 012111.

[33] H. P. Komsa, A. V. Krasheninnkov, *J. Phys. Chem. Lett.* **2012**, *3*, 3652.

[34] G. Kresse, J. Furthmüller, *Comput. Mat. Sci.* **1996**, *6*, 15.

[35] A. Togo, F. Oba, I. Tanaka, *Phys. Rev. B* **2008**, *78*, 134106.

[36] K. P. Odonnell, X. Chen, *Appl. Phys. Lett.* **1991**, *58*, 2924–2926.

[37] S. Tongay, J. Zhou, C. Ataca, K. Lo, T. S. Matthews, J. B. Li, J. C. Grossman, J. Q. Wu, *Nano Lett.* **2012**, *12*, 5576–5580.

[38] W. H. Weber, R. E. Merlin, *Raman Scattering in Materials Science*, Springer-Verlag, Berlin **2000**.

[39] Y. Liang, L. Zhai, X. Zhao, D. Xu, *J. Phys. Chem. B* **2005**, *109*, 7120–7123.

[40] S. Pagliara, L. Sangaletti, L. E. Depero, V. Capozzi, G. Perna, *Solid State Commun* **2000**, *116*, 115–119.

[41] K. Motobayashi, Y. Kim, H. Ueba, M. Kawai, *Phys. Rev. Lett.* **2010**, *105*, 076101.

[42] T. Kato, T. Matsumoto, T. Ishida, *Jpn J. Appl. Phys. 1* **1988**, *27*, 983–986.

[43] M. I. Alonso, K. Winer, *Phys. Rev. B* **1989**, *39*, 10056–10062.

[44] T.-T. Kang, A. Hashimoto, A. Yamamoto, *Phys. Rev. B* **2009**, *79*, 033301.

[45] D. O. Dumcenco, K. Y. Chen, Y. P. Wang, Y. S. Huang, K. K. Tiong, *J. All. Comp.* **2010**, *506*, 940.